Yang et al., http://www.jcb.org/cgi/content/full/jcb.200605053/DC1

Supplemental results

The NPC activity under improved transport conditions

In earlier work where we demonstrated that single-molecule fluorescence microscopy could be used to determine interaction times for an IC consisting of NLS-2xGFP(2C), Imp α, and Imp β (Yang et al., 2004), the import efficiency was not estimated because we were unable to determine from which aqueous compartment the cargo entered the NPC and to which aqueous compartment it went after leaving the NPC. This experimental limitation arose mainly because the rapid three-dimensional diffusion of the cargo within the cytoplasmic and nucleoplasmic compartments precluded tracking the cargo before and after interaction with an NPC. Here, we have used a brighter cargo (NLS-2xGFP[4C]; four cysteines for dye labeling instead of two), increased the frame rate (from 333 to 500 or 1,000 frames per second [fps]) with higher camera sensitivity (approximately twofold), and increased the solution viscosity (by approximately twofold) through addition of 25% glycerol.

Control experiments suggested that our improved conditions did not significantly alter NPC properties or cargo interactions with the NPC or transport cofactors. These control experiments are summarized as follows: (1) The interaction time was independent of the dye on the cargo (Alexa 555 or 647), the number of dye molecules on the cargo (2 or 4), and the viscosity (0 or 25% glycerol in the import buffer; Fig. S1, A–D). (2) Based on viscosity differences, the bulk transport rate in the 25% glycerol buffer was expected to be approximately two- to threefold slower than that in the import buffer without glycerol (see below). Initial bulk transport rates in the absence and presence of 25% glycerol differed by ~1.5–3-fold (Fig. S1 E). These results are therefore consistent with the expected difference in diffusion constants under the different viscosity conditions. There are, however, some caveats. First, in our experience, errors in initial rate measurements using confocal microscopy arise because of the difficulty of obtaining instantaneous concentration jumps at the coverslip surface. The laminar flow effects were

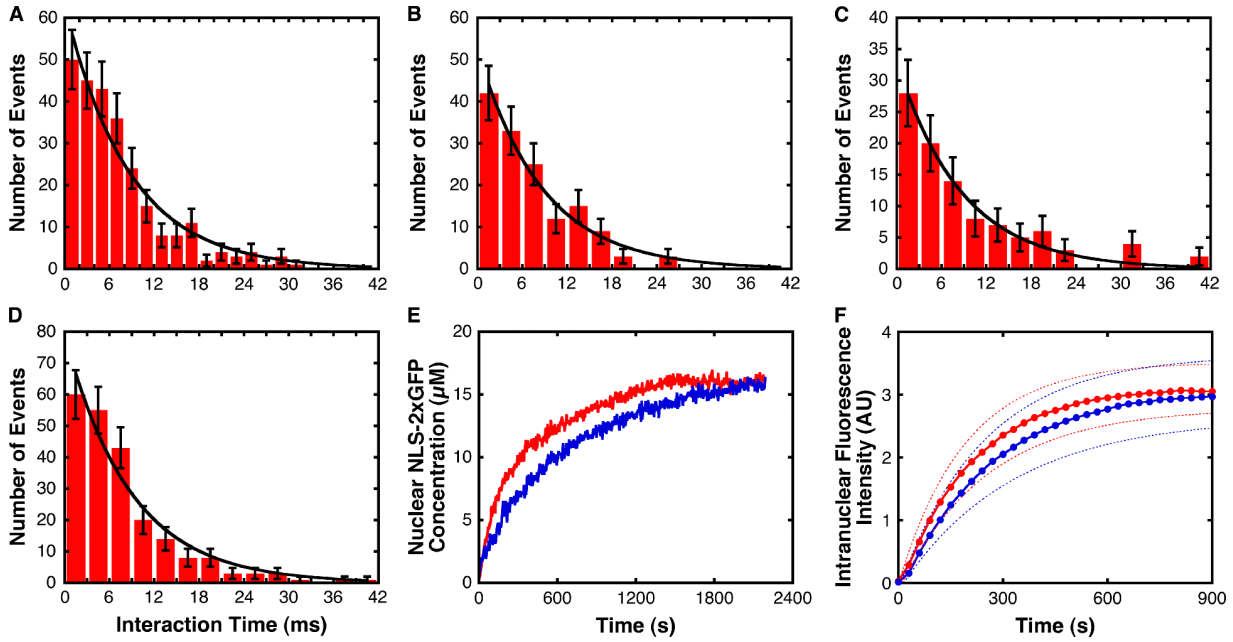

Figure S1. **Interaction times for different dyes, numbers of dye molecules, and bulk viscosities.** Interaction times were measured under conditions in which the dye on the cargo (Alexa 555 or 647), the number of dye molecules on the cargo (2 or 4), or the bulk viscosity (0 or 25% glycerol in import buffer) was varied: A and B indicate that the interaction time was independent of the dye molecule; A and C indicate that the interaction time was independent of the viscosity; and B and D indicate that the interaction time was independent of the number of dye molecules on the cargo. Conditions were the same as in Fig. 1, unless otherwise indicated. (A) Interaction time histogram of NLS-2xGFP(4C) labeled with four Alexa 647 molecules in import buffer with 25% glycerol. $\tau = 8.6 \pm 0.4$ ms; $n = 264$; 500 fps. (B) Interaction time histogram of NLS-2xGFP(4C) labeled with four Alexa 555 molecules in import buffer with 25% glycerol. $\tau = 8.7 \pm 0.7$ ms; $n = 145$; 333 fps. (C) Interaction time histogram of NLS-2xGFP(4C) labeled with four Alexa 647 molecules in import buffer. $\tau = 8.7 \pm 0.6$ ms; $n = 97$; 333 fps. (D) Interaction time histogram of NLS-2xGFP(2C) labeled with two Alexa 555 molecules in import buffer. $\tau = 8.8 \pm 0.6$ ms, $n = 231$; 333 fps (data from Yang et al., 2004). (E) Nuclear accumulation of NLS-2xGFP(4C) in the presence and absence of 25% glycerol measured by confocal microscopy. (red) 0% glycerol; (blue) 25% glycerol. [Alexa555-NLS-2xGFP] = [Imp α] = [Imp β] = 1.5 μM. (F) Nuclear accumulation of dye-labeled and unlabeled NLS-2xGFP(4C) in import buffer measured by epifluorescence microscopy. The GFP fluorescence was used to monitor the kinetics of nuclear transport for (red) unlabeled NLS-2xGFP(4C) and (blue) NLS-2xGFP(4C) labeled with four Alexa 555 molecules. Shown is the intranuclear fluorescence intensity after subtracting the cytoplasmic background. The dashed lines indicate the standard deviation envelope for measurements from 4 (red) or 6 (blue) nuclei. [cargo] = 0.5 μM.

TABLE S1. Summary of Results from Single Molecule Nuclear Import Experiments

	Interaction Time (ms)	*n* (for Interaction Time)	Import Efficiency (%)	*n* (for Import Efficiency)	Interaction Frequency (events s^{-1} μm^{-1})
IC Concentration:[1]					
0.0001 μM	8.6±0.4	264	51±5	100	2.2±0.2
1.5	4.5±0.3	217	57±6	72	2.5±0.2
5.0	2.9±0.1	171	63±6	71	2.1±0.2
10	2.2±0.2	169	69±6	70	2.6±0.3
15 (2 ms)	2.2±0.1	262	77±5	87	2.4±0.2
(1 ms)	2.3±0.3	195	76±5	78	2.2±0.3
Imp β Concentration:					
0.1 μM	8.2±0.9	253	50±5	101	2.0±0.5
0.5	8.6±0.4	264	51±5	100	2.4±0.2
1.0	3.8±0.3	193	57±6	75	2.3±0.2
1.5	2.8±0.2	185	59±6	68	2.1±0.2
5 (2 ms)	1.8±0.1	195	72±5	75	2.4±0.5
(1 ms)	1.7±0.1	258	72±4	95	2.5±0.2
10 (2 ms)	1.3±0.1	227	76±5	76	2.6±0.2
(1 ms)	1.4±0.1	219	77±4	106	2.8±0.3
15 (2 ms)	1.2±0.1	322	82±4	107	2.6±0.2
(1 ms)	1.1±0.1	326	82±4	124	2.8±0.2
NLS-2xGFP(2C) labeled with two Alexa647 molecules; [Imp β] = 15 μM:					
(1 ms)	1.3±0.2	200	79±4	96	2.8±0.3
[Imp β] = 1.5 μM; [Ran] = 6 μM; [NTF2] = 3 μM:					
	2.3±0.1	256	58±5	86	2.4±0.3
[Imp β] = 0.5 μM; values measured 15-16 min after reaction initiation:					
(1 ms)	1.9±0.1	175	71±6	65	2.8±0.3
RanGAP Concentration ([Imp β] = 15 μM):					
0 μM (2 ms)	1.2±0.1	322	82±4	107	2.6±0.2
(1 ms)	1.1±0.1	326	82±4	124	2.8±0.2
1.5 (2 ms)	1.6±0.1	178	74±5	68	2.7±0.3
(1 ms)	1.6±0.1	164	73±6	64	2.8±0.1
5	2.1±0.1	148	68±6	66	2.6±0.2
10	3.6±0.1	183	67±6	73	2.5±0.1
15	4.2±0.2	181	61±6	75	2.3±0.2

RanBP1 Concentration ([Imp β] = 3 μM; [RanGAP] = 0.5 μM):					
0 μM (1 ms)	1.9±0.1	235	68±5	88	2.6±0.2
0.5 μM (1 ms)	2.5±0.2	212	70±5	80	2.6±0.5
1 μM (1 ms)	3.4±0.3	193	66±6	67	2.8±0.5
2 μM (1 ms)	4.3±0.2	204	66±6	73	2.4±0.4
4 μM (1 ms)	4.6±0.4	236	64±5	91	2.5±0.2
RanBP1 Concentration ([Imp β] = 15 μM; [RanGAP] = 0.5 μM):					
0 μM (1 ms)	1.4±0.1	256	81±5	64	2.6±0.2
0.5 μM (1 ms)	1.3±0.1	215	82±4	81	2.4±0.3
1 μM (1 ms)	1.2±0.1	201	82±4	77	2.7±0.2
2 μM (1 ms)	1.4±0.1	192	81±5	73	2.2±0.2
4 μM (1 ms)	1.3±0.1	238	83±5	103	2.2±0.3
Imp β/RanGAP Concentrations (1 mM GMP-PNP):					
0.5 μM/0 μM	3.7±0.2	261	63±5	90	2.2±0.2
15 μM/0 μM (1 ms)	1.3±0.1	214	78±5	80	2.6±0.2
15 μM/15 μM (1 ms)	1.2±0.1	204	80±5	82	2.5±0.1
In Vivo (microinjection pipette contained 0.1 nM fCargo):					
NLS-2xGFP(4C)[2]	7.8±0.4	307	51±5	115	1.5±0.1
10 KD dextran (2 ms)	1.8±0.1	284	50±4	136	3.5±0.3
(1 ms)	1.8±0.1	374	50±4	141	3.8±0.2
rPOM121-EGFP3-tagged NPCs ([Imp β] = 0.5 μM):					
	2.1±0.1	169	62±6	65	1.9±0.1
10 kD dextran (0.1 nM); import buffer + 25% glycerol (unless otherwise noted):					
0 μM Imp β, no glycerol	2.2±0.1	170	not determined		6.5±0.3
0 μM Imp β (2 ms)	2.2±0.2	184	51±6	70	6.7±0.3
(1 ms)	2.2±0.3	130	50±7	52	6.6±0.3
0.5 μM Imp β (1 ms)	1.1±0.1	280	67±4	110	6.8±0.4
1.5 μM Imp β (1 ms)	0.5±0.1 (≤0.5)[3]	154	68±6	68	3.8±0.5
3 μM Imp β (1 ms)	0.5±0.1 (≤0.5)[3]	168	67±7	64	2.3±0.3

rpS13 (0.1 nM); import buffer + 25% glycerol (unless otherwise noted):					
0 μM Imp β, no glycerol	3.3±0.1	161	not determined		4.5±0.3
0 μM Imp β	3.2±0.3	171	50±6	67	4.3±0.3
	τ (ms)	**t_{ave} (ms)**	***n***		
[Imp β] = 0.5 μM:[4]					
IT	8.6±0.4	8.4±0.6	264		
TT_t	8.0±0.4	8.0±1.2	51		
TT_a	8.6±0.7	8.3±1.1	49		
[Imp β] = 15 μM:[4]					
IT (2 ms)	1.2±0.1	1.4±0.1	322		
(1 ms)	1.1±0.1	1.2±0.1	326		
(combined)[5]	1.1±0.1	1.4±0.1	648		
TT_t (2 ms)	1.2±0.1	1.4±0.1	88		
(1 ms)	1.1±0.1	1.2±0.1	101		
(combined)[5]	1.0±0.1	1.4±0.1	189		
TT_a (2 ms)	1.9±0.2	1.7±0.3	19		
(1 ms)	1.6±0.3	1.2±0.1	23		
(combined)[5]	1.4±0.1	1.5±0.1	42		

The model cargo was NLS-2xGFP(4C) labeled with four Alexa 647 molecules, except as noted and in the rpS13 and dextran experiments. Except for the rpS13, dextran, and in vivo experiments, the GTP, Ran, NTF2, Imp α and fluorescent cargo (fCargo) concentrations were 1 mM, 2 μM, 1 μM, 0.5 μM, and 0.1 nM, respectively, unless otherwise indicated. Nonfluorescent cargo (nfCargo) was only added in the IC concentration experiments. Except where indicated, all in vitro experiments used import buffer + 25% glycerol. 3–5 nuclei per measurement are reported. Values were measured 1–2 min after reaction initiation, unless otherwise noted. The time resolution was 2 ms, unless otherwise noted. For all interaction times ≤2 ms, values were measured at 1,000 fps. In some cases, interaction times measured at both 500 fps (2 ms/frame) and 1,000 fps (1 ms/frame) are reported. Errors represent 68% confidence intervals.

[a]All cargo was assumed to be part of an IC at the start of the experiment. For the 0.0001 μM value, [IC] ≈ [fCargo] = 0.1 nM, [nfCargo] = 0 μM, [Imp α] = [Imp β] = 0.5 μM. For all other values, [IC] ≈ [nfCargo] = [Imp α] = [Imp β], [fCargo] = 0.1 nM.

[b]Pooled data obtained at 333 fps (cargo labeled with four Alexa 555 molecules) and 500 fps (cargo labeled with four Alexa 647 molecules).

[c]For interaction times ≤0.5 ms, lower interaction frequencies suggest that some shorter events were missed and therefore the measured interaction times are upper limits. The interaction time obtained from the data is given, but the fact that this is an upper limit is noted in parentheses.

[d]Values for IT (mean interaction time), TT_t (true transport time), and TT_a (abortive transport time) were determined from a single exponential fit (τ) and by a simple mean (t_{ave} ± SEM). For single exponential data where τ is greater than the frame duration, τ and t_{ave} should yield values to within 4% for sufficiently high *n*; τ is expected to be ~12% less than t_{ave} when τ is about half the frame duration (the case for 500 fps and 15 μM Imp β). The t_{ave} is less sensitive than τ to small values of *n*.

[e]Data collected at 500 and 1,000 fps was "combined" to yield a single data set with 2-ms bins. The combined data does not simply yield an average of the two data sets because of different *n* values, round-off error, and the fact that information is lost upon conversion of 1-ms data into 2-ms bins.

most serious for higher viscosity buffers. Second, the relatively lengthy time required for the NE Ran concentration to reach steady state (Fig. 4) suggests an additional significant source of error in initial rate measurements under these conditions. (3) The permeability barrier still existed and the same equilibrium cargo concentration gradient was maintained between the nucleus and cytoplasm in the presence and absence of glycerol (Fig. S1 E). Because equilibrium concentration gradients do not rely on rapid mixing, these values are considered more accurate than initial rates. Of course, it is conceivable that multiple rate constants could be altered by 25% glycerol, yielding the identical equilibrium cargo concentration gradient. (4) A similar nuclear accumulation rate and equilibrium cargo concentration gradient was observed for cargo with and without the Alexa 555 dye labels (Fig. S1 F), suggesting that the dye labels do not affect transport. (5) Interaction frequency was expected to be dependent on a particle's diffusion constant. Thus, it was expected that the interaction frequency of ICs in the presence of import buffer plus 25% glycerol would be about half that in import buffer without glycerol because of the approximate twofold difference in diffusion constants that is expected to result from the viscosity differences (see below). The interaction frequency of the 10-kD dextran and rpS13 were similar in the presence and absence of glycerol (Table S1). The interaction frequency of NLS-2xGFP was approximately twofold higher in the presence of 25% glycerol than in its absence (Table S1; Yang et al., 2004). These data indicate that productive collisions with the NPC were approximately two- to fourfold more likely in the presence of 25% glycerol. It is unclear whether the higher productive collision rate in 25% glycerol resulted from changes in NPC structure and/or affinities or from differential accessibilities to the NPC through the remaining cytoskeletal structure within the cytoplasmic compartment.

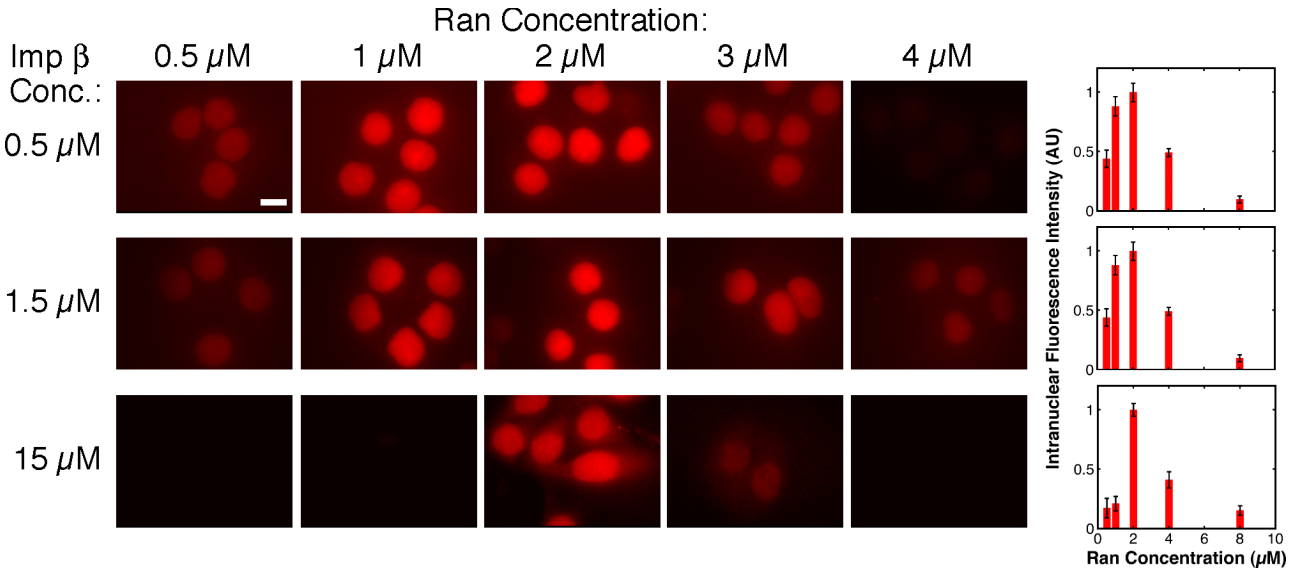

Figure S2. **Ran is dominant-negative at high concentrations in bulk transport assays.** The nuclear accumulation after 10 min of NLS-2xGFP(4C) labeled with four Alexa 555 molecules was measured by epifluorescence microscopy at various concentrations of Ran, Imp β, and NTF2. The Ran and Imp β concentrations are noted above the columns or to the left of rows of images, respectively. The NTF2 concentration was half of the Ran concentration. All images within a row were scaled identically. The graph to the right of each row shows the normalized intranuclear intensity after subtracting the cytoplasmic background (a value of 0, therefore, indicates that the cytoplasmic and nuclear fluorescence intensities were identical). [Alexa555-NLS-2xGFP] = 0.2 μM; [Imp α] = 0.5 μM; [GTP] = 1 mM. Bar, 10 μm.

Homogeneity of fluorescent cargo preparations

Maleimides can react with thiols and amines but are typically much more reactive toward thiols. Our data suggest that the frequency of amine-dye coupling was small within our cargo preparations. As detailed earlier (Yang and Musser, 2006), the saturation of dye labeling occurred consistently with the numbers of reactive cysteines on the cargo. Single-molecule photobleaching experiments revealed that with four reactive cysteines on the cargo, the vast majority of cargos had four or fewer dye molecules attached. When there were only two reactive cysteines on the cargo, the vast majority of cargos were labeled by two or fewer dye molecules. With regards to labeling an amine in or near the NLS and its possible effect on transport activity, transport was inhibited by dye labeling a cysteine near the NLS (unpublished data). These data suggest that dye labeling an amino acid residue in or near the NLS would inhibit transport. The transport of NLS-2xGFP(4C) was not inhibited by dye labeling (Fig. S1 F), consistent with the hypothesis that the amines within the NLS were not labeled significantly. Finally, the NLS-2xGFP cargo labeled with two or four dye molecules had similar interaction times and transport efficiencies, and the interaction time histograms were well fit by a single exponential (Fig. S1 and Table S1). These data support the hypothesis that our cargo preparations were reasonably homogeneous. In total, our data support the hypothesis that amine labeling was insignificant under our conditions and that the vast majority of the reactive cysteines were tagged with dye molecules. Thus, fluorescent cargo preparations were reasonably homogeneous.

Effect of dyes on binding affinities

Multiple possible interactions could potentially be affected by dye labeling of the cargo, but our data suggest that these interactions were minimally affected by the dye molecules. For example, the interaction of the cargo with Imp α could be affected by the dye molecules on the cargo because of steric constraints. In FRET experiments using Alexa 647–labeled cargo and Alexa 555–labeled Imp α (approximately four dye molecules on each protein), the K_d was estimated to be 44 ± 4 nM in the presence of 500 nM Imp β (Sun, C., personal communication). For comparison, published data indicate a K_d for this interaction of ~40 nM (Catimel et al., 2001). These data suggest that the cargo–Imp α interaction was minimally affected by our dye labeling techniques. A second possibility is that the chemical properties (e.g., the hydrophobicity) of the dye molecules on the cargo could affect the interaction between the cargo import complex and the NPC, most likely its interaction with the network of FG-Nups. This interaction cannot be probed with isolated NPC components because the physical properties of the intact FG-Nup network are critical to establishing the physiological interaction. Nonetheless, the cargo's NPC interaction time, import efficiency, and NPC interaction frequency were not affected by the number or identity of the dye molecules on the cargo (Fig. S1 and Table S1). These data argue against the hypothesis that the number and/or identity of the dyes on the cargo in our experiments significantly affected the affinity of the import complex for the NPC. Thus, the data currently in hand support the hypothesis that dye labeling of the cargo did not significantly affect its behavior during nuclear transport.

Optimal Ran concentration

High concentrations of Ran inhibit the bulk nuclear accumulation efficiency of the NLS-2xGFP cargo in in vitro assays. In our hands, the optimal Ran concentration was ~2 μM at both low and high concentrations of Imp β (Fig. S2). Thus, 2 μM Ran was used for the vast majority of our single-molecule measurements.

Diffusion constants from single-particle tracking measurements

Although it is generally agreed that the cytoplasmic viscosity is higher than that of pure water (1 cP), estimates of cytoplasmic viscosity vary widely depending on the method used, the probe, and the cell type (Goulian and Simon, 2000; Luby-Phelps, 2000; Wachsmuth et al., 2000; Kues et al., 2001). As a control to the applicability of in vitro transport measurements to in vivo results, we determined the viscosities of the buffers used and the HeLa cell cytoplasm. Our approach was as follows: (1) the diffusion constant, D, was determined for an IC in solutions of known viscosity, η; (2) these measurements allowed us to calculate the effective radius (r_{eff}) of the IC using the Stokes-Einstein relation ($D = kT/6\pi\eta r_{eff}$); and (3) knowing the r_{eff}, the viscosities of unknown solutions were estimated by determining D, and using the Stokes-Einstein relation was used to estimate η.

Diffusion constants were determined from the distance traveled between video frames using single-particle tracking methods (Yang et al., 2004). For a particle diffusing in two dimensions, the displacement, δ, of the particle during a series of equally space time intervals, τ, follows the frequency distribution $p(\delta, \tau, D) = (\delta/2D\tau) \exp(-\delta^2/4D\tau)$ (Smith et al., 1999; Kues et al., 2001). Thus, we tracked freely diffusing particles in dilute solution within a single focal plane and fit the histogram of the displacements observed when images were collected at 500 fps to the above frequency distribution. With this approach, an IC in import buffer plus 25% glycerol yielded $D = 17.6 \pm 1.0$ $\mu m^2/s$ (Fig. S3 A). To estimate the viscosity from this diffusion constant, it is necessary to know the effective radius, r_{eff}, of the particle. Thus, IC diffusion constants were determined in a series of solutions of known viscosities. Fitting these data with the Stokes-Einstein relation yielded an r_{eff} for the IC of 3.6 nm (Fig. S3 B). This value is in good agreement with the expected radius of the IC (~4 nm), assuming a sphere of mass equal to an IC. Using this value for r_{eff}, the viscosity of the solution used for most of the reported transport experiments (import buffer + 25% glycerol) was calculated from D (Fig. S3 A) as 3.5 $\pm$ 0.2 cP. We were unable to obtain a reliable estimate of the viscosity of pure import buffer by these methods because of poor localization precision that was due to rapid diffusion under these conditions. Traditional viscosity measurements using a falling ball-type viscometer proved unreliable, presumably because the PVP polymer in the solution generated surface effects due to polymer-surface interactions. We estimate that PVP increased the viscosity of import buffer lacking PVP from ~1 cP (pure water) to ~1.2-1.7 cP (import buffer; contains 1.5% PVP). Thus, bulk transport rates should be ~2.1- to 2.9-fold slower in the presence of import buffer + 25% glycerol (~3.5 cP) compared with import buffer without glycerol (~1.2-1.7 cP).

The in vivo behavior of the NLS-2xGFP cargo was then examined within ~4 μm of the NE on the cytoplasmic side after microinjection into live cells. We assumed that the cargo rapidly assembled into an IC. Two diffusion constants were required to fit the data, and each accounts for ~50% of the particles: D_1 (53%) = 1.4 $\pm$ 0.2 $\mu m^2/s$; D_2 (47%) = 9.4 $\pm$ 0.7 $\mu m^2/s$ (Fig. S3 C). The diffusion constant associated with the slower moving particles (D_1) is consistent with that of substantially immobilized particles (e.g., stuck within a macromolecular cage or transiently adhered to a substantially immobilized particle). For comparison, cargos adsorbed on a coverslip surface, and thus completely immobilized, yielded $D = 0.10 \pm 0.01$ $\mu m^2/s$ (though D is theoretically zero for an immobilized particle, a nonzero D results from a nonzero precision). The diffusion constant associated with the faster moving particles (D_2) was assumed to correspond to a freely diffusing IC. Thus, from D_2, the apparent cytoplasmic viscosity was estimated as 6.5 $\pm$ 1.2 cP.

From the trajectories in Fig. 2 A, the diffusion constants of the IC when interacting with the NPC and in the cytoplasmic compartment were estimated as 0.9 $\pm$ 0.1 and 9.2 $\pm$ 0.7 $\mu m^2/s$, respectively. Thus, the diffusion constant of the cargo within the NPC (expected to be predominantly present as part of an IC) was significantly smaller than that of the IC on the cytoplasmic side of the NE. This measured diffusion constant within the NPC applies only to the low Imp β concentration condition and is likely an underestimate of the true diffusion constant because the particle was confined. The in vitro cytoplasmic diffusion constant (9.2 $\pm$ 0.7 $\mu m^2/s$) was significantly smaller from that within pure import buffer + 25% glycerol (17.6 $\pm$ 1.0 $\mu m^2/s$; Fig. S3 A). Crowding and steric effects resulting from the remaining cytoskeletal structure in permeabilized cells likely explains this result (Luby-Phelps, 2000). Notably, the in vitro cytoplasmic diffusion constant (9.2 $\pm$ 0.7 $\mu m^2/s$;

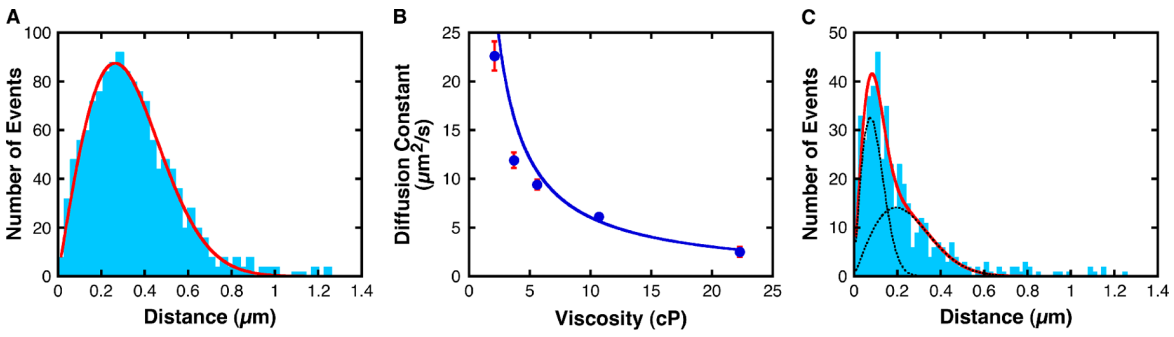

Figure S3. **Viscosity estimates from single-molecule diffusion measurements.** The fluorescent cargo was NLS-2xGFP(4C) labeled with four Alexa 647 molecules. (A) Frequency distribution of the distance traveled by an IC in 2 ms in import buffer + 25% glycerol. The data were fit to $p(\delta, \tau, D) = (\delta/2D\tau) \exp(-\delta^2/4D\tau)$, yielding a diffusion constant of 17.6 $\pm$ 10 $\mu m^2/s$. [Imp α] = [Imp β] = 0.5 μM; [fluorescent cargo] = 0.1 nM. (B) Diffusion constants of an IC in solutions of known viscosities. The solutions used were import buffer lacking PVP with 25, 40, 50, 60, and 70% glycerol. We assumed that the salts and buffering agent present in the solution did not significantly alter the viscosity from tabulated values for glycerol solutions (Lide, 1998). [Imp α] = [Imp β] = 0.5 μM; [fluorescent cargo] = 0.1 nM. (C) Frequency distribution of the distance traveled in 2 ms by cargo microinjected into live HeLa cells. Data were fit to $p(\delta, \tau, D_1, D_2) = A*p(\delta, \tau, D_1) + B*p(\delta, \tau, D_2)$ (red), where A and B are weighting factors for the two component frequency distributions (black).

import buffer + 25% glycerol) was statistically indistinguishable from the in vivo value (9.4 ± 0.7 $\mu m^2/s$; Fig. S3 C). Thus, we conclude that our single-molecule transport experiments were conducted under viscosity conditions that closely resemble those found in vivo.

Viscosity within the putative central channel

The microviscosity within the putative central channel through which signal-independent cargos are proposed to transit (Macara, 2001; Peters, 2005) could potentially be significantly different from that of the bulk viscosity because of the channel's small dimensions (diameter of ~10.8 nm and length of ~45 nm [Keminer and Peters, 1999]). Two possible corrections to estimate the viscosity within the putative central channel were considered. First, viscosities within narrow channels can be significantly higher than in bulk solution because of the ordering of water molecules by the channel edges. Consequently, diffusion within such narrow channels could be significantly slower than that expected from the bulk solution viscosity. However, significant viscosity effects are expected to be only significant for channel diameters less than ~2.5 nm (Liu et al., 2004). Thus, the mean viscosity within a 10.8-nm-wide channel should not be substantially larger than that of the bulk solution. Second, because the PVP (360 kD) used in the import buffer + 25% glycerol solution is significantly larger than the size-exclusion limit of the NPC (20–40 kD), the viscosity within the putative central channel is expected to be less than the viscosity of import buffer + 25% glycerol (~3.5 cP) in all the reported in vitro experiments.

NPCs tagged with GFP on POM121

As a test of the accuracy of our NE localization procedure in bright-field images (Yang et al., 2004), we used the same procedure to identify the path of the NE from fluorescent NPCs. HeLa cells (Yang et al., 2004) were stably transfected with rPOM121-EGFP3 (plasmid was a gift from J. Ellenberg, European Molecular Biology Laboratory, Heidelberg, Germany; Rabut et al., 2004) using Lipofectamine 2000 (Invitrogen) to fluorescently tag the NPCs (Fig. S4). The root mean square difference in the position of the NE determined by bright-field and rPOM121-EGFP3 fluorescence imaging was 15 ± 5 nm (n = 5 nuclei), with the position of the NE from the fluorescent images on the inside of the position determined from the bright-field images. The exact position of POM121 in the NPC is not known, although it is certainly cen-

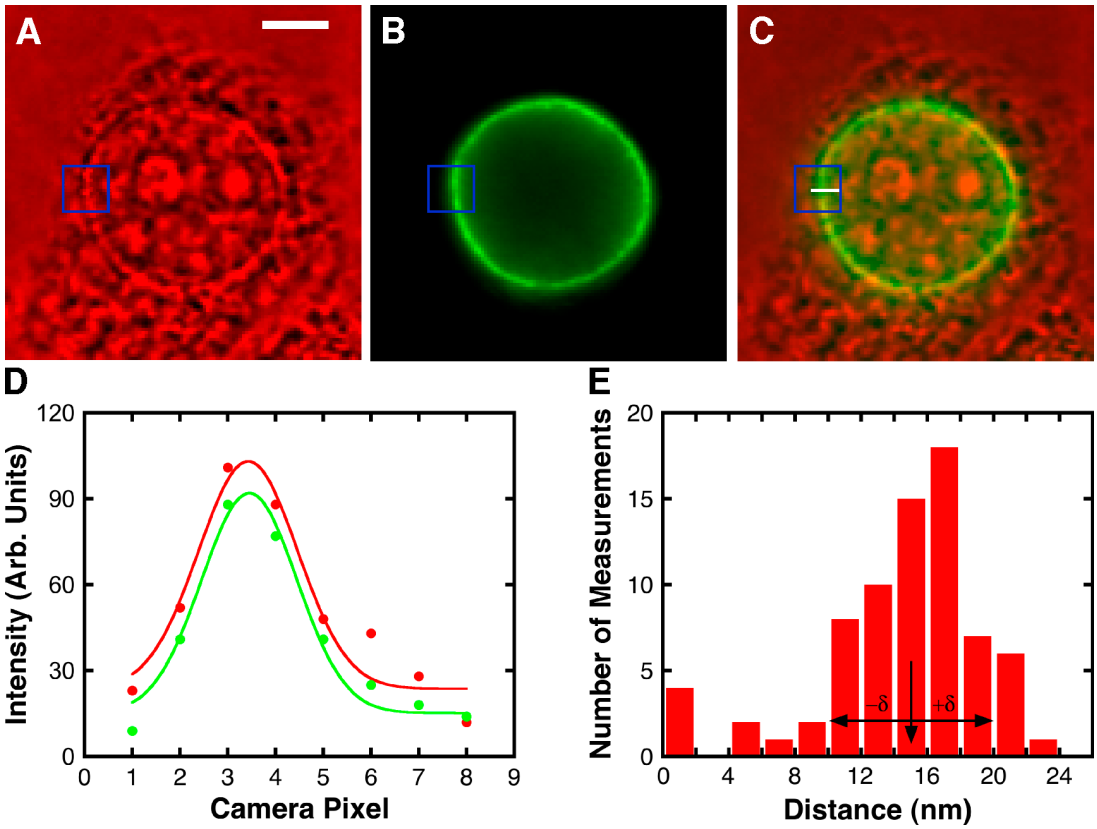

Figure S4. **Localization of the nuclear envelope by bright-field and fluorescence imaging.** False-color bright-field (A), fluorescence (B), and merged images (C) of a HeLa cell transfected with rPOM121-EGFP3. The position of the NE was determined where the NE in the bright-field image was easily identifiable, e.g., in the boxed region; only such regions were used for single-molecule experiments. Bar, 5 µm. (D) Intensity profile of a typical line scan across the NE from the bright-field (red) and fluorescence (green) images in A and B. The white line in C identifies the position of the line scan. The data are fit to a Gaussian; the peak position identifies the position of the NE in the row of pixels. To zero the axes, 19 pixels were subtracted from x-axis values, and 90 intensity units were subtracted from y-axis values. (E) Distribution of the differences in NE positions in rows of pixels from the bright-field and fluorescence imaging methods. A positive distance indicates that the position of the NE determined from the fluorescence image is inside (more toward the center of the nucleus) the position of the NE as determined from the bright-field image. The mean and SD of the distribution are identified by the arrows. n = 5 nuclei.

trally located (Söderqvist et al., 1997). Because the bright-field and fluorescence methods yielded similar and reproducible results, either is appropriate, in principle, for NE localization as long as the method (i.e., the point of reference) is noted.

Our criteria to categorize trajectories (i.e., as class 1, 2, or 3; see Materials and methods) are expected to depend on the NE localization procedure because the inclusion of points from a trajectory depends on distance from the NE. In addition, the interaction time depends on accurate assignment of trajectory points as arising from a diffusing cargo or one that is interacting with an NPC. The fact that the interaction time estimated here at very low cargo and low Imp β concentrations was indistinguishable from the interaction time determined earlier when we could not observe the freely diffusing cargo (Yang et al., 2004) suggests that our selection criteria for cargo interaction with NPCs was reasonably accurate. Further, using the fluorescent POM121-based NE localization procedure instead of the bright-field–based procedure, but retaining the same trajectory selection criteria for inclusion in import efficiency calculations (i.e., shifting the "NPC interaction region" by 15 nm), led to similar results (within the errors of the measurements). Thus, our methods are reasonably robust.

An altered pore occupancy condition could be created by covalent tethering of nontransport cofactor protein domains within the FG-Nup network. We tested this possibility by measuring the NLS-2xGFP interaction time and import efficiency for NPCs that had GFP domains attached to POM121. POM121 contains FG-repeat domains at its C terminus (Söderqvist et al., 1997); thus, C-terminally-linked GFP domains are expected to be embedded within the FG network. Previous studies with rat kidney cells (NRK) indicated 47 ± 20 GFP domains per NPC when the cells were transfected with rPOM121-EGFP3 (Rabut et al., 2004). The bright NEs observed in our HeLa cells expressing rPOM121-EGFP3 are consistent with the hypothesis that a large number of GFP domains were present in the NPCs in these cells (Fig. S4 B). In vitro measurements at a very low cargo concentration (0.1 nM) yielded an interaction time and import efficiency of 2.1 ± 0.1 ms and 62 ± 6%, respectively. These values represent an approximately fourfold decrease in interaction time and an increase in import efficiency (from 51 to 62%) from wild-type NPCs (compare with Fig. 3 A at 0.1 nM IC). These data are consistent with the hypothesis that an increased mass of material in the pore leads to a decreased interaction time and an increased import efficiency. Alternatively, the GFP domains on POM121 could have perturbed the NPC structure and thereby influenced the interaction time and import efficiency. Because these data indicate that the GFP tags on POM121 significantly affected the functional properties of the NPC, we used the bright-field NE localization procedure and performed all of our single-molecule transport experiments on wild-type cells (with the exception of the rPOM121-EGFP3 experiments described above).

Difference between transport time and interaction time

Because we were able to distinguish the side of the NE from which a cargo entered an NPC and to which it exited that NPC, we were able to estimate a true transport time. The (mean) interaction time is a general summary statistic that includes NE interaction times for cargos that transported, those that underwent abortive transport, and those that approached within 100 nm of a known NPC location, but for which no other information may have been known. In contrast, the transport time is a more precise summary statistic because it is calculated only from the interaction times estimated from trajectories that clearly cross the NE. In principle, abortive transport times could be different from entry (true) transport times. For most of the conditions reported herein, the interaction times for entry and abortive events were the same within experimental error (Fig. 2, B and C). However, occasional differences (statistically significant according to fit errors) were observed (Fig. 3, C and D). Despite statistical insignificance in most cases, the time constants for abortive transport were consistently ~0.2–0.6 ms larger than those for entry transport over the range of conditions examined, suggesting that abortive transport does take slightly longer than entry transport. This possibility can be explained by a picture in which ICs are predominantly dissociated near the nucleoplasmic face of the NPC and release of cargo to the cytoplasmic compartment takes slightly longer on average than release to the nucleoplasmic compartment because of the greater distance that must be traveled. If there truly exists differences between entry and abortive transport times (e.g., that could be unequivocally resolved by higher resolution measurements), these differences must be small (equal to or less than ~0.6 ms). Thus, for simplicity, we generally report only the mean interaction times.

Precision of interaction times

To confirm the validity of interaction times near or less than the frame integration time of 2 ms, 1 ms/frame temporal resolution was used to repeat some experiments. For 15 μM ICs (Fig. 3 A), interaction times of 2.2 ± 0.1 ms (n = 262) and 2.3 ± 0.3 ms (n = 195) were obtained with 500 and 1,000 fps acquisition rates, respectively. Similarly, interaction times of the 10-kD dextran were 2.2 ± 0.2 (n = 184) and 2.2 ± 0.3 (n = 130) using the same image acquisition rates, respectively. Table S1 list five independent measurements of interaction times between ~1.1 and ~1.8 ms at both 500 and 1,000 fps. In all cases, the two time resolutions gave virtually identical results. These data indicate that accurate interaction time measurements were obtained for interaction times as short as about half the frame integration time. It may seem counterintuitive that interaction times shorter than the time resolution could be reliably estimated. However, because the interaction times followed exponential distributions, there were measurements made that were longer than the time resolution. Thus, it was really the number of measurements at the longer times (bins ≥ 2) compared with the number of measurements at the time resolution (bin 1) that determined the interaction time (except, of course, in cases where the interaction time was much faster than the time resolution, e.g., the 10-kD dextran at 15 μM Imp β).

Precision of spatial localization

The spatial localization precision for immobile NLS-2xGFP(4C) particles labeled with four Alexa 647 molecules was 15 ± 4 nm (n = 20) at 500 fps and 36 ± 3 nm (n = 20) at 1,000 fps. These values represent improvements from earlier measurements (Yang et al.,

2004) because of an increase in signal-to-noise ratio (*S*/*N*) for three main reasons: (1) greater photon output (4 vs. 2 dyes; (2) a more sensitive camera; and (3) image filtering with a 3 × 3 Gaussian kernel. The localization precision for a moving particle is inherently less than that of a stationary particle. Assuming that the localization error due to movement alone is at most approximately half the distance the particle diffuses during image acquisition (Yang and Musser, 2006), we estimate that the precision with which cargos were localized when interacting with the NPC was equal to or less than ~40–50 nm.

Mechanistic explanations for changes in the interaction time and import efficiency

The exact mechanism whereby the Imp β concentration influences interaction time and import efficiency is likely to be complex. We first consider a direct role for Imp β in modulating interaction time. At higher bulk Imp β concentrations, greater numbers of Imp β molecules were observed at the NE (Fig. 5), consistent with the hypothesis that a greater number of Imp β molecules were bound within the FG-Nup network under these conditions. A large number of cargo-free Imp β molecules within the FG network reduces the volume available to transiting molecules. Although the volume occupied by Imp β cannot be calculated without knowing the volume of the FG network or whether the volume of this network expands to accommodate Imp β (or other) molecules, we estimate that the network volume occupied by Imp β molecules could be significant (tens of percent volume) under some of the investigated transport conditions. A decreased available volume implies a lower entropy and, thus, an increased free energy for transiting molecules in the pore, which in turn suggests easier access to the rate-limiting transition state and, hence, faster escape (Minton, 2001). A higher number of Imp β molecules within the FG network reduces the number of available IC binding sites and, thus, also predicts a lower entropy for ICs within the FG network. Thus, simple thermodynamics predicts that, in the absence of other rate-determining factors, a molecule should exit the NPC faster when the FG network is occupied by a larger number of Imp β molecules. In principle, the concentration of other transport complexes or transport cofactors in the NPC could similarly affect a cargo's interaction time. Under the conditions of our experiments, the concentration of Imp β at the NE varied most significantly.

We next consider a few indirect mechanisms whereby Imp β may influence a signal-dependent cargo's interaction time. First, because release of an Imp α/β–dependent cargo from the NPC is rate limited by RanGTP (Yang et al., 2004), an increase in the rate of cargo release from the NPC could result from faster interaction of ICs with RanGTP molecules. We showed that an increase in the Imp β concentration at the NE does not correlate with an increase in the Ran concentration at the NE (Figs. 4 and 5). Thus, higher concentrations of Imp β do not simply recruit additional Ran molecules to the NPC. However, the RanGTP/RanGDP ratio and/or the Ran distribution within the NPC could change as a result of an increased Imp β concentration within the NPC. And second, Imp β likely disrupts energetically favorable filament interactions (Ribbeck and Görlich, 2001). Thus, high Imp β concentrations could increase the fluidity of the FG network (and hence the diffusion constant of the IC). Such structural perturbations might, therefore, change the RanGTP distribution within the FG network or promote an increased productive interaction rate between ICs and RanGTP.

Until now, we have suggested mechanisms by which the interaction time could vary with Imp β concentration in the NPC. Though interaction time and import efficiency are not determined by the same set of parameters, the general principle determining changes in these transport characteristics is likely to be the same: namely, pore occupancy modulates thermodynamic and/or kinetic barriers within the NPC, which in turn differentially affects interaction time and import efficiency. It is unclear at this juncture how interaction time and transport efficiency are varied to different extents under different conditions.

References

Catimel, B., T. Teh, M.R.M. Fontes, I.G. Jennings, D.A. Jans, G.J. Howlett, E.C. Nice, and B. Kobe. 2001. Biophysical characterization of interactions involving importin α during nuclear import. *J. Biol. Chem.* 276:34189–34198.

Goulian, M., and S.M. Simon. 2000. Tracking single proteins within cells. *Biophys. J.* 79:2188–2198.

Keminer, O., and R. Peters. 1999. Permeability of single nuclear pores. *Biophys. J.* 77:217–228.

Kues, T., R. Peters, and U. Kubitscheck. 2001. Visualization and tracking of single protein molecules in the cell nucleus. *Biophys. J.* 80:2954–2967.

Lide, D. 1998. CRC Handbook of Chemistry and Physics. D.R. Lide, editor. CRC Press, Boca Raton, FL. 2496 pp.

Liu, Y., Q. Wang, and L. Lu. 2004. Transport properties and distribution of water molecules confined in hydrophobic nanopores and nanoslits. *Langmuir*. 20:6921–6926.

Luby-Phelps, K. 2000. Cytoarchitecture and physical properties of cytoplasm: volume, viscosity, diffusion, intracellular surface area. *Int. Rev. Cytol.* 192:189–221.

Macara, I.G. 2001. Transport into and out of the nucleus. *Microbiol. Mol. Biol. Rev.* 65:570–594.

Minton, A.P. 2001. The influence of macromolecular crowding and macromolecular confinement on biochemical reactions in physiological media. *J. Biol. Chem.* 276:10577–10580.

Peters, R. 2005. Translocation through the nuclear pore complex: selectivity and speed by reduction-of-dimensionality. *Traffic*. 6:421–427.

Rabut, G., V. Doye, and J. Ellenberg. 2004. Mapping the dynamic organization of the nuclear pore complex inside single living cells. *Nat. Cell Biol.* 6:1114–1121.

Ribbeck, K., and D. Görlich. 2001. Kinetics analysis of translocation through nuclear pore complexes. *EMBO J.* 20:1320–1330.

Smith, P.R., I.E.G. Morrison, K.M. Wilson, N. Fernandez, and R.J. Cherry. 1999. Systems analysis of Ran transport. *Biophys. J.* 76:3331–3344.

Söderqvist, H., G. Imreh, M. Kihlmark, C. Linnman, N. Ringertz, and E. Hallberg. 1997. Intracellular distribution of an integral nuclear pore membrane protein fused to green fluorescent protein: localization of a targeting domain. *Eur. J. Biochem.* 250:808–813.

Wachsmuth, M., W. Waldeck, and J. Langowski. 2000. Anomalous diffusion of fluorescent probes inside living cell nuclei investigated by spatially-resolved fluorescence correlation spectroscopy. *J. Mol. Biol.* 298:677–689.

Yang, W., J. Gelles, and S.M. Musser. 2004. Imaging of single-molecule translocation through nuclear pore complexes. *Proc. Natl. Acad. Sci. USA.* 101:12887–12892.

Yang, W., and S.M. Musser. 2006. Visualizing single molecules interacting with nuclear pore complexes by narrow-field epifluorescence microscopy. *Methods*. 39:316–328.